Carrier mobility of highly transparent conductive Al-doped ZnO polycrystalline films deposited by radio-frequency, direct-current, and radio-frequency-superimposed direct-current magnetron sputtering: Grain boundary effect and scattering in the grain bulk

Junichi Nomoto,[a] Hisao Makino, and Tetsuya Yamamoto
Research Institute, Kochi University of Technology, 185 Miyanokuchi, Tosayamada-cho, Kami-shi, Kochi 782-8502, Japan

(Received 16 August 2014; accepted 7 January 2015; published online 23 January 2015)

The effects of using radio-frequency (RF)-superimposed direct-current (DC) magnetron sputtering deposition on the structural, electrical, and optical properties of aluminum-doped ZnO (AZO)-based highly transparent conducting oxide films have been examined. AZO films were deposited on heated non-alkaline glass substrates (200 °C) using ZnO:Al_2O_3 (2 wt. % Al_2O_3) ceramic oxide targets with the total power varied from 150 to 300 W, and at various RF to DC power ratios, AZO films deposited by a mixed approach with the RF to the total power ratio of 0.14 showed the lowest resistivity of 2.47×10^{-4} Ω cm with the highest carrier concentration of 6.88×10^{20} cm^{-3} and the highest Hall mobility (μ_H) of 36.8 cm^2/Vs together with the maximum value of an average transmittance in the visible spectral range from 400 to 700 nm. From the analysis of optical data based on the simple Drude model combined with the Tauc-Lorentz model and the results of Hall effect measurements, the optical mobility (μ_{opt}) was determined. A comparison of μ_{opt} with μ_H clarified the effects of the mixed approach not only on the reduction of the grain boundary contribution to the carrier transport but also on retaining high carrier mobility of in-grains for the AZO films. [http://dx.doi.org/10.1063/1.4906353]

I. INTRODUCTION

Zinc oxide (ZnO) with a wurtzite structure is a versatile material with a wide band gap of 3.37 eV at room temperature. Highly transparent conductive Al- or Ga-doped ZnO (AZO or GZO) films have in recent years been rediscovered as a subject of considerable research interest owing to their distinctive physical properties: low electrical resistivity (ρ) of 2×10^{-4} to 4×10^{-4} Ω cm and high visible (VIS) transmittance of more than 80% for glass substrates coated with the films and their wide range of possible electronic and optical applications as an alternative to tin-doped indium oxide (In_2O_3:Sn) and fluorine-doped tin oxide (SnO_2:F).[1–4]

An issue to be resolved for their wide application is to develop a deposition technique to control carrier mobility. Industrial coating processes have reached a highly advanced level in terms of process equipment. One widely used technique is magnetron sputtering (MS) deposition method, in which direct current (DC) power is usually applied, often yielding good material quality at a reasonably high deposition rate and moderate cost.[2,5] Another widely employed technique is radio frequency (RF) MS deposition (RF-MS), which is used to deposit highly insulating materials.[6] In the RF processes, there is enhanced substrate bombardment by plasma ions, such as Ar^+ of moderate energy,[7] which can assist grain growth, leading to denser films with high crystallinity. A drawback of the RF processes, however, is the lower sputtering rates that result from the lower discharge voltage.[8] An interesting alternative is to add a certain amount of RF power to the applied DC power; a technique known as RF-superimposed DC-MS (RF/DC-MS), which has favorable effects on the growth of transparent conductive oxides, such as ITO,[9–13] AZO,[14–17] GZO,[18,19] and In-doped ZnO (IZO).[20] This technique also enables the control of surface roughness,[4,10] a requirement that is particularly important for displays. Cross-sectional images of GZO films deposited by RF/DC-MS or DC-MS obtained by transmission electron microscopy (TEM) reveal that GZO films deposited by RF/DC-MS have a smoother surface than GZO films deposited by DC-MS, while both polycrystalline GZO films consist of columnar grains with the *c*-axis oriented normal to the surface of the glass substrate.[4]

In our previous work, we reported the benefits of RF/DC-MS on the electrical properties of polycrystalline GZO films with a carrier concentration (N) of 1.03×10^{21} cm^{-3}. The Hall mobility (μ_H) of 14.26 cm^2/Vs, determined by Hall effect measurements, was similar to that of polycrystalline GZO films with a lower N of 0.63×10^{21} cm^{-3} deposited by DC-MS on glass substrates.[4] In comparison, polycrystalline GZO films deposited by ion plating with dc-arc discharge on glass substrates exhibited a lower ρ with a higher μ_H of 22.20 cm^2/Vs together with $N = 1.02 \times 10^{21}$ cm^{-3}, similar to that of the above GZO films deposited by RF/DC-MS on glass substrates. The above GZO films deposited by three different deposition techniques at a glass substrate temperature of 180 °C had a thickness of 100 nm.

[a]Electronic mail: nomoto.junichi@kochi-tech.ac.jp

Highly transparent conductive films made from ZnO films deposited using the industrially scalable MS technique have polycrystalline structure. That is, the film is composed of many small regions, called grains that have different orientations of the crystal structure. Between the grains are grain boundaries (GBs), which are regions of extreme disorder in the crystal structure. In such films, we usually face an important problem, which is to elucidate the effect of the GBs on carrier transport. We require a comprehensive understanding of the effects of the above deposition techniques on the carrier mobility in the grain bulk (μ_{ig}) and at GBs (μ_{GB}).[21–25] To obtain low-ρ AZO films with high transmittance in the VIS region, a deposition technique should be developed to produce films with not only high μ_{ig} values but also little contribution of the GBs to carrier transport, μ_{ig}/μ_{GB}, together with N on the order of $10^{20}\,\mathrm{cm}^{-3}$ to suppress free-carrier absorption in a wide wavelength range in the VIS region.

In the present study, we investigated the structural, electrical, and optical properties relevant to the carrier mobility of polycrystalline AZO films deposited by three different MS methods, DC-MS, RF-MS, and RF/DC-MS, to clarify the factors that determine carrier transport in polycrystalline AZO films. We analyzed AZO films deposited by systematically varying the total power (the sum of the DC power (P_{DC}) and RF power (P_{RF})) as well as the ratio of P_{RF} to the total power.[9,19] We determine the critical power ratio at which rapid changes in the structure, such as the lattice parameters and the alignment of columnar grains, occur. The results are correlated with the electrical properties of AZO films and compared with the contribution of the GB scattering mechanism to carrier transport estimated by theory combined with optical experimental data. We also clarify the characteristics of polycrystalline AZO films deposited by conventional DC-MS or RF-MS in terms of the contribution of GB scattering to the carrier transport. In the following, we demonstrate the features of the highly transparent conductive AZO films deposited by MS at the critical power ratio.

II. EXPERIMENTAL DETAILS

We deposited 500-nm-thick AZO films on glass substrates (Corning Eagle XG) at a substrate temperature of 200 °C by three different MS deposition methods: DC-MS, RF-MS, and RF/DC-MS. The oxide targets (Tosoh Corp.) were high-density sintered circular AZO targets (diameter: 80 mm) prepared with an Al_2O_3 content of 2.0 wt. %. We used a MS apparatus (ULVAC CS-L) with a sintered oxide target. The nine different deposition processes using the various MS techniques mentioned above are summarized in Table I. DC-MS (Proc. 1) and RF-MS (Proc. 9) were conducted with a P_{DC} of 200 W and an P_{RF} of 200 W, respectively. The RF/DC-MS processes, from Proc. 2 to Proc. 8, were carried out by adding an RF component in the power range of 10–200 W to an applied P_{DC} of 50–150 W. Details of the various ratios of P_{RF} to the total power ($P_{DC}+P_{RF}$) are given in Table I.

All deposition processes were carried out in a pure argon (Ar) atmosphere at a pressure of 1.0 Pa. Prior to deposition, the chamber was evacuated until the base pressure reached about 2.0×10^{-5} Pa. The substrate was rotated at a velocity of 10 rpm during the deposition. A substrate with an area of $100\times100\,\mathrm{mm}^2$ was placed parallel to the target surfaces with a minimum substrate-target distance of 100 mm.

The properties of AZO films were evaluated for samples obtained by cutting the center area of the glass substrates with deposited AZO films into $10\times10\,\mathrm{mm}^2$ pieces. The film thickness was measured using surface a profilometer (KLA Tencor, Alpha-Step IQ). The crystal structure of the AZO films was characterized by high-resolution (HR) x-ray diffraction (XRD) using Cu-Kα (wavelength $\lambda=0.1540562$ nm) radiation (Rigaku, ATX-G). The out-of-plane XRD pattern (synchronous scan of 2θ and ω in the horizontal plane), in-plane XRD pattern (synchronous scan of $2\theta\chi$ and ϕ in the azimuth plane), and out-of-plane rocking curve (2θ-fixed ω scan) were obtained. The ρ, N, and μ_H for the AZO films at room temperature were determined by Hall effect measurements with the van der Pauw method (Nanometrics, HL5500PC). The optical transmittance and reflectance spectra of the AZO films in the wavelength range from 200 to 2400 nm were obtained by a spectrophotometer (Hitachi, U-4100) with an incident angle of light of 5°.

III. RESULTS AND DISCUSSION

A. Deposition properties

Figure 1(a) shows the DC sputtering voltage (V_{DC}) on the target (discharge voltage) as a function of the power ratio, $P_{RF}/(P_{DC}+P_{RF})$, during the deposition. We found a

TABLE I. Process number, DC power (P_{DC}), RF power (P_{RF}), total power ($P_{DC}+P_{RF}$), ratio of P_{RF} to total power ($P_{RF}/(P_{DC}+P_{RF})$), and deposition rate in unit of nm/min.

Process number	P_{DC} [W]	P_{RF} [W]	Total power ($P_{DC}+P_{RF}$) [W]	Power ratio $P_{RF}/(P_{DC}+P_{RF})$	Deposition rate [nm/min]
Proc. 1	200	0	200	0.00	11
Proc. 2	150	10	160	0.06	6.8
Proc. 3		25	175	0.14	7.9
Proc. 4		50	200	0.25	9.1
Proc. 5	100	100	200	0.50	7.6
Proc. 6		200	300	0.67	13
Proc. 7	50	100	150	0.67	5.1
Proc. 8		200	250	0.80	8.8
Proc. 9	0	200	200	1.00	8.2

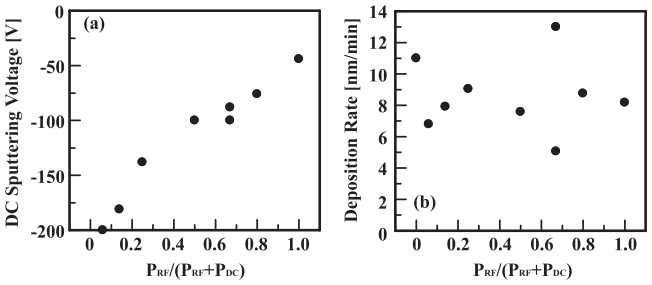

FIG. 1. (a) DC sputtering voltage and (b) deposition rate as a function of the power ratio, $P_{RF}/(P_{DC}+P_{RF})$.

strong relationship between V_{DC} and the power ratio; the absolute value of V_{DC} decreased monotonically from 200 to 44 V with increasing power ratio from 0.06 to 1.0.[16,19] This was due to the difference between the DC and RF discharge processes.[8,26] In the case of MS deposition, DC discharge is sustained by secondary electrons emitted from the target surface. Therefore, the linear increase in the secondary emission coefficient with the incident ion energy results in a high V_{DC}.[27] The collision of negative ions with higher collision energy with the film, induced by a higher V_{DC}, can damage the film during its growth. On the other hand, the RF discharge is driven by ionization through electrons that undergo oscillating motion in plasma. Considering that RF discharge excitation is much more effective than ionization by non-oscillating secondary electrons, the enhanced plasma density due to the superimposition of RF in the DC process should reduce V_{DC}. In other words, the role of the superimposition of RF in the DC process is to increase the plasma density, which reduces V_{DC}. Reducing V_{DC} can be very effective for reducing the damage to films caused by negative ions.[28]

Figure 1(b) shows that the deposition rate drops significantly when only 6% RF power is added to the DC process. For the RF-superimposed DC processes, we found that the deposition rate remained almost constant except for the two different processes with $P_{RF}/(P_{DC}+P_{RF})=0.67$, Proc. 6 and Proc. 7. From Table I, these processes had maximum and minimum of total powers $(P_{DC}+P_{RF})=300$ W (Proc. 6) and $P_{DC}+P_{RF}=150$ W (Proc. 7), respectively. The highest and lowest deposition rates were obtained at this value of $P_{RF}/(P_{DC}+P_{RF})$, as can be seen in Fig. 1(b). Note that the deposition rate was not a dominant factor determining the properties of the films in our experiment. We later discuss which factors limit the properties of AZO films in terms of $P_{RF}/(P_{DC}+P_{RF})$ as a dominant parameter in order to clarify which deposition process provides highly transparent conductive AZO films with high carrier mobility.

B. Structural properties

The out-of-plane and in-plane XRD patterns show that all the films deposited by the different deposition techniques have a wurtzite structure. No peaks indicating other phases, such as crystalline Al oxides or Zn metal, were observed. Figure 2 shows the out-of-plane XRD patterns of AZO films deposited with various power ratios, $P_{RF}/(P_{DC}+P_{RF})$, indicating the effect of the RF/DC-MS technique on the film structure, seen as from the changes in the main ZnO diffraction

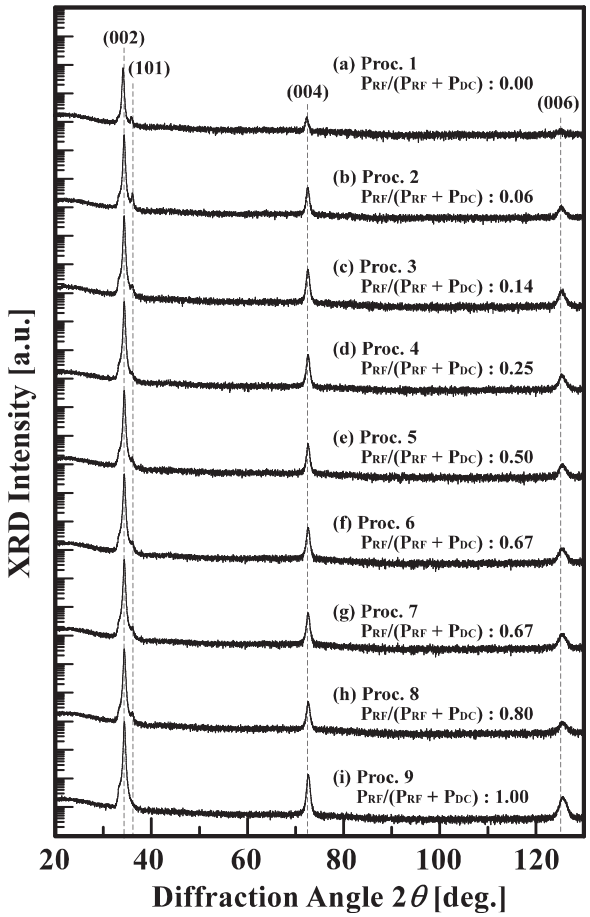

FIG. 2. Out-of-plane XRD patterns of AZO films deposited with various power ratios.

peaks. From the analysis of the out-of-plane XRD patterns, for all the samples, the wurtzite ZnO (002) peak (i.e., at 2θ of approximately 34.4°) was found to be much higher than the other peaks in the diffraction patterns. We found that deposition by the RF/DC-MS processes improved the crystallinity to produce marked increases in the (002), (004), and (006) peak intensities.

On the basis of this finding, we can further compare the three samples deposited by Proc. 1, Proc. 5, and Proc. 9. The AZO films deposited with $P_{RF}/(P_{DC}+P_{RF})=0.0$, i.e., only by DC-MS, show poor crystallinity: the (002) and (004) peak intensities are very weak compared with those of the other samples and a very small peak of (006) diffraction can be observed. The AZO films with a mixed grain orientation exhibited a peak at $2\theta=36.18°$, which corresponds to the (101) peak in the vicinity of the (002) peak at $2\theta=34.47°$. Note that the (101) plane is a high-density crystal plane showing the maximum diffraction intensity in the pattern of bulk powder ZnO (JCPDS #36–1451) with a random phase pattern. For the AZO films deposited with $P_{RF}/(P_{DC}+P_{RF})=0.14$, we found that the (002) peak shifted to a higher angle of $2\theta=34.48°$ and had strong intensity, whereas the peak centered at 36.18°, corresponding to the (101) peak, had diminished intensity. On the other hand, for the AZO films deposited with $P_{RF}/(P_{DC}+P_{RF})=1.0$, corresponding to only the RF-MS method, we found a sharp (002) peak shifted to

an even higher angle of $2\theta = 34.53°$, together with not only an increase in the intensities of both the (004) and (006) peaks but also a complete absence of the (101) reflection. These AZO films have a well-defined single (0001) orientation. It appears that in this case, the RF plasma itself carried some internal stress that induced preferential growth.

These findings indicate the following: (1) a high V_{DC} may induce some internal stress, which can change the energetic balance between the (002) and (101) orientations compared with that of stress-free ZnO-based powders,[29] which is discussed below in terms of the lattice constants; (2) the increase in the power ratio, which reduces V_{DC} by increasing the plasma density caused by the superimposition of RF to DC (Fig. 1(a)), induces the preferential growth of AZO films in the (002) direction, resulting in the improved crystallinity of AZO films oriented along the *c*-axis.

Figure 3 shows the full width at half maximum (FWHMω) of the (002) rocking curve ω plotted as a function of the power ratio, $P_{RF}/(P_{DC}+P_{RF})$. It clearly demonstrates that the superimposition of RF to DC induced a change in the *c*-axis alignment between the columnar grains of the polycrystalline structure. For the AZO films deposited with $P_{RF}/(P_{DC}+P_{RF}) = 0.0$, corresponding to DC-MS, the largest FWHMω value of 13.7 was obtained. In such films, however, the large FWHMω value was meaningless considering that the (002) peak pattern was mixed with the (101) peak pattern, as shown in Fig. 2. RF/DC-MS improved the *c*-axis alignment between columnar grains oriented perpendicular to the substrate. Upon increasing $P_{RF}/(P_{DC}+P_{RF})$ to 0.14, we found a large reduction in the FWHMω value. Upon further increasing $P_{RF}/(P_{DC}+P_{RF})$ to 0.8, FWHMω tended to increase slightly, which was followed by a sharp fall when $P_{RF}/(P_{DC}+P_{RF})$ was increased to 1.0. We found that the lowest FWHMω value of 3.96 with a strong (002) peak (Fig. 2) was obtained for the AZO films deposited with $P_{RF}/(P_{DC}+P_{RF}) = 1.0$, corresponding to RF-MS.

The in-plane XRD patterns of AZO films deposited with $P_{RF}/(P_{DC}+P_{RF}) = 0.0$, 0.14 and 1.0 are shown in Figs. 4(a)–4(c), respectively. Figures 4(b) and 4(c) show that the

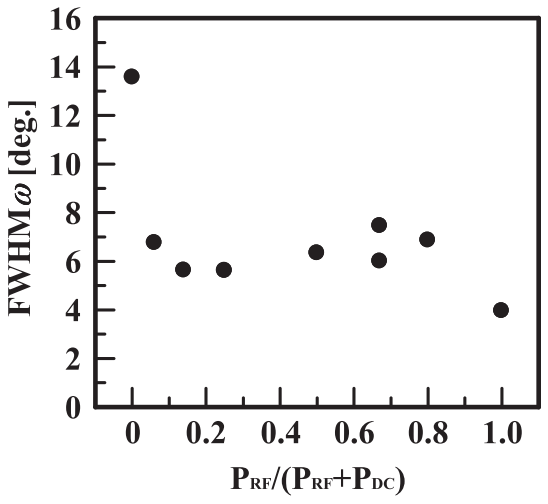

FIG. 3. FWHMω of the (002) rocking curve ω of AZO films as a function of the power ratio, $P_{RF}/(P_{DC}+P_{RF})$.

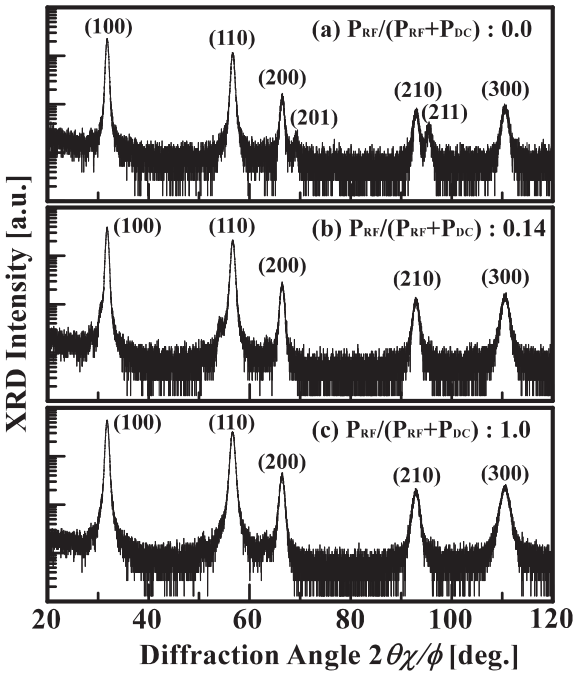

FIG. 4. In-plane XRD patterns of AZO films deposited with power ratios, $P_{RF}/(P_{DC}+P_{RF})$, of (a) 0.0, (b) 0.14, and (c) 1.0.

AZO films deposited with $P_{RF}/(P_{DC}+P_{RF}) = 0.14$ and 1.0 exhibited peaks at $2\theta\chi$ values of ~31.8°, 56.6°, 66.4°, 93.0°, and 110°, in good agreement with the JCPDS card (No. 36–1451) for a typical wurtzite ZnO crystal, which correspond to the (100), (110), (200), (210), and (300) planes, respectively. The in-plane XRD patterns show that the AZO films deposited under these different deposition conditions exhibited a preferential *c*-axis orientation perpendicular to the substrate. On the other hand, for the AZO films deposited with $P_{RF}/(P_{DC}+P_{RF}) = 0.0$, i.e., by only DC-MS, we found peaks corresponding to the (201) and (211) planes, in addition to the five planes above, at $2\theta\chi$ values of ~69.1° and 95.3°, respectively (JCPDS card (No. 36-1451)), as shown in Fig. 4(a). These AZO films were polycrystalline with poor *c*-axis orientation compared with the AZO films deposited by RF/DC-MS or RF-MS because of the mixed grain.

Analysis of the data obtained by out-of-plane and in-plane XRD measurements shows that RF/DC-MS and RF-MS play an important role in enhancing the crystal quality of polycrystalline AZO films with a preferential orientation along the *c*-axis perpendicular to the glass substrate.

As the next step, we investigated the $P_{RF}/(P_{DC}+P_{RF})$ dependence of the *a*-axis and *c*-axis parameters (l_a and l_c) and the volume of the unit cell (V) in the AZO films. Figure 5 shows (a) l_a and l_c and (b) V for AZO films as a function of $P_{RF}/(P_{DC}+P_{RF})$. l_a and l_c were estimated from the (100) and (002) peak positions in the in-plane and out-of-plane XRD patterns, respectively. V was calculated from the lattice parameters. As shown in Fig. 2, with increasing $P_{RF}/(P_{DC}+P_{RF})$, 2θ for the (002) plane shifted to a higher angle (34.53°) resulting from the decrease in the lattice parameter d, i.e., the spacing between adjacent (002) planes, in accordance with Bragg's law. Figure 5(a) shows that l_c (=2d) decreased

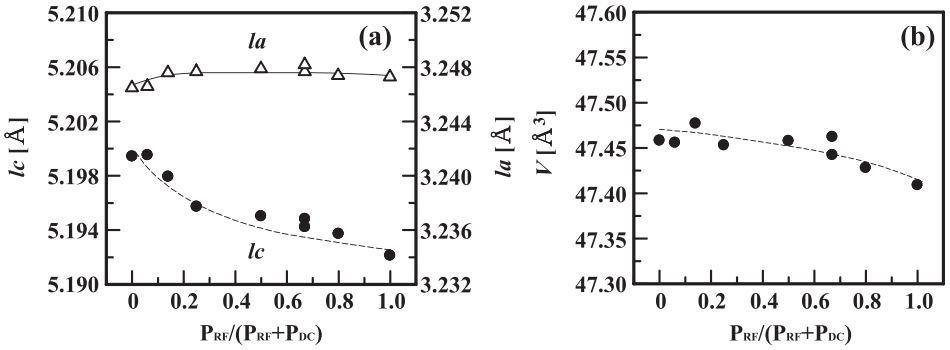

FIG. 5. (a) a-axis and c-axis lattice parameters (l_a and l_c) and (b) unit-cell volume V of AZO films as a function of the power ratio, $P_{RF}/(P_{DC}+P_{RF})$.

from 5.1995 to 5.1921 Å when $P_{RF}/(P_{DC}+P_{RF})$ increased from 0.0 to 1.0, which can be explained by the compressive strain along the c-axis direction. Note that with increasing $P_{RF}/(P_{DC}+P_{RF})$ up to 0.14, l_c showed a sharp fall. On the other hand, as $P_{RF}/(P_{DC}+P_{RF})$ increased, l_a maintained a value of about 3.247 Å, resulting in V ($\propto l_a \times l_a \times l_c$) decreasing from 47.4582 to 47.4088 Å^3. No experiments to obtain the information on the lattice parameters of stress-free AZO powders with the same Al content incorporated into the films in this study have been reported, to the best of our knowledge. In our previous work, we discussed the dependence of the residual stress on film thicknesses for GZO films by a comparison of the lattice parameters between GZO films with various film thicknesses and stress-free GZO powders with the same Ga content incorporated into the films.[24] Further discussion on the dependence of the residual-stress behavior in the films on $P_{RF}/(P_{DC}+P_{RF})$ on the basis of the biaxial stress models is required.

The AZO films deposited by RF-MS, which exhibited a well-defined single (0001) orientation, had the lowest values of V. Taking into account the fact that the AZO films also show the best c-axis alignment between the columnar grains of the polycrystalline structure, it suggests that the concentration of Zn and/or Al interstitials, n-type defects that would lead to an increase in V at a high doping level, in the grain is very low in the AZO films compared with in other samples. Electrical properties strongly depend on the level of intrinsic and/or extrinsic defects associated with the Al doping density and on the contribution of GB scattering mechanism to carrier transport. As a consequence of these observations of the dependence of structural properties on $P_{RF}/(P_{DC}+P_{RF})$, we determined the critical power ratio of which marked structural changes occur to be 0.14.

C. Electrical properties

Figure 6 shows (a) ρ and (b) N and μ_H plotted against $P_{RF}/(P_{DC}+P_{RF})$. Figure 6(a) shows that as the power ratio increased from 0.0, corresponding to DC-MS, ρ reached a minimum of 2.47×10^{-4} Ωcm at $P_{RF}/(P_{DC}+P_{RF}) = 0.14$. ρ gradually increased up to a power ratio of 0.8, above which it decreased; the ρ value of AZO films deposited at $P_{RF}/(P_{DC}+P_{RF}) = 1.0$, corresponding to RF-MS, was approximately 4.37×10^{-4} Ω cm. Figure 6(b) shows that N increased up to a power ratio of 0.14, above which it decreased gradually; N had a maximum of 6.88×10^{20} cm^{-3} at $P_{RF}/(P_{DC}+P_{RF}) = 0.14$. We found the $P_{RF}/(P_{DC}+P_{RF})$ dependence of μ_H to be similar to that of N with increasing $P_{RF}/(P_{DC}+P_{RF})$ up to 0.8. When $P_{RF}/(P_{DC}+P_{RF})$ was further increased to 1.0, μ_H increased abruptly. ρ was thus lowest for the AZO films deposited by Proc. 3, which resulted from the highest N together with most improved μ_H.

Figure 6(b) shows that N drastically changed with the power ratio. For AZO films deposited by RF-MS, which has the best crystallinity as shown in Fig. 2, we found the minimum value of N. For n-type AZO films, possible dominant defects include intrinsic n-type defects, such as oxygen vacancy (V_o) and Zn interstitial (Zn_i) together with Al species substituting Zn sites (Al_{Zn}). We must consider the effects of the combination of those intrinsic defects with the extrinsic defects on the microstructure, such as crystallinity and V and N. Analysis of data obtained by *ab initio* electronic band structure calculations shows that the generation of V_o decreases V, whereas the formation of Zn_i with various

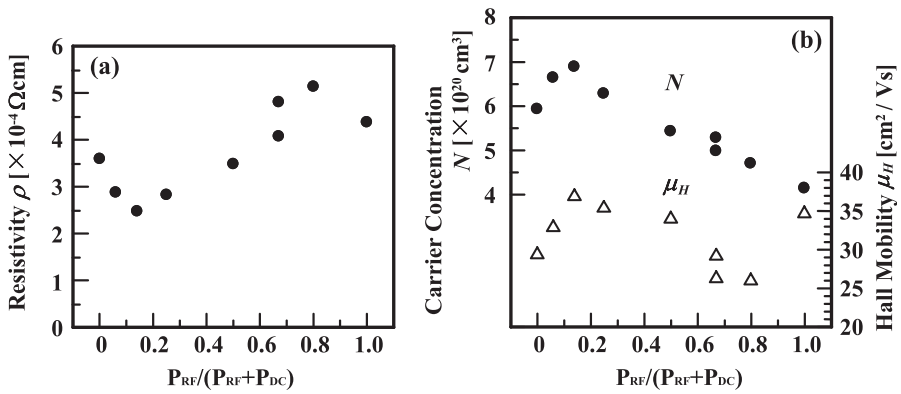

FIG. 6. (a) Electrical resistivity ρ and (b) carrier concentration N and Hall mobility μ_H of AZO films as a function of the power ratio, $P_{RF}/(P_{DC}+P_{RF})$.

interstitial locations, which gives rise to the deterioration of the crystallinity, increases it.[30] Note that V_o can be a deep donor in ZnO, whereas Zn_i produces a shallow donor level below the bottom of the conduction.[31] Taking into account the fact that the V decreased and the crystallinity increased with $P_{RF}/(P_{DC}+P_{RF})$ increased from 0.0 to 1.0 (See Figs. 2 and 5(b)), we came to the logical deduction that the ratio of $n(Zn_iAl_{Zn})/n(V_oAl_{Zn})$ decreased with increasing $P_{RF}/(P_{DC}+P_{RF})$. $n(Zn_iAl_{Zn})$ and $n(V_oAl_{Zn})$ denote the density of the defect-combination, respectively. It explains well that the N value of AZO films deposited at $P_{RF}/(P_{DC}+P_{RF})=1.0$ exhibited very low compared with AZO films deposited at $P_{RF}/(P_{DC}+P_{RF})=0.0$, in spite of the best crystallinity (see Fig. 2).

D. Optical properties

The optical measurements of the AZO films yielded several interesting results. Analysis of the optical data showed that all the AZO films in this work exhibited an average optical transmittance (T) exceeding 84% in the VIS region (400–700 nm). Figure 7 shows the T and reflectance (R) of glass substrates with AZO films deposited by three different processes, Proc. 1, Proc. 3, and Proc. 9, as a function of wavelength (λ). The average T (T_{av}) values of the samples deposited by Proc. 1, Proc. 3, and Proc. 9 were 84.4, 84.7, and 84.2%, respectively. Note that the AZO films deposited by Proc. 3 with the lowest ρ had the highest T_{av} among all the samples in this work.

In the near-infrared (NIR) spectral range from 0.8 to 2.4 μm, T decreased with increasing λ, whereas R abruptly increased after showing a deep minimum as shown in Fig. 7. Taking into account the fact that the value of R for a material with refractive index n and extinction coefficient k is given by $R=((n-1)^2+k^2)/((n+1)^2+k^2)$, R reaches a low value at λ_m corresponding to $n\cong 1$ provided k^2 is small. Note that whether or not k^2 is small in the vicinity of λ_m depends on the carrier relaxation time. Analysis of the T and R curves based on the Drude model provides us with the optical mobility (μ_{opt})[32,33] as discussed in Sec. III F.

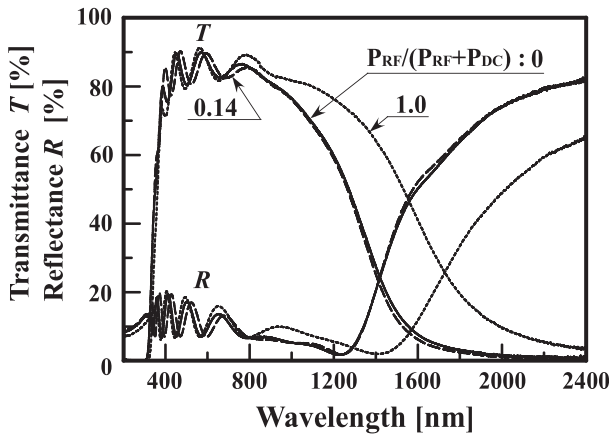

FIG. 7. Optical transmittance (T) and reflectance (R) spectra of AZO films deposited with $P_{RF}/(P_{DC}+P_{RF})$ ratio of 0.0, 0.14, and 1.0.

E. Scattering mechanism and compensation in grain bulk

The free-carrier absorption coefficient α is characterized by a monotonic spectrum that grows as $\alpha \propto \lambda^p$, where λ is the photon wavelength and the exponent p depends on the dominant optical scattering mechanism; the scattering by acoustic phonons and polar optical phonons give dependences of $\lambda^{1.5}$,[34] and $\lambda^{2.5}$,[35] respectively, whereas the scattering by ionized impurities gives $p=3$–3.5, depending on the approximations used in the theory.[36] This means that the effect of electrically charged scattering centers is to produce absorption with stronger frequency dependence than that resulting from lattice vibration. In the AZO films with different power ratios, all three modes of scattering are expected to occur and the resultant α will be a weighted sum of the three different processes.

Table II shows process number, power ratio, N, absorption coefficient at $\lambda=1400$ nm (α_{1400}), the capture cross section (α_{1400}/N), best fitting p, fitting region, correlation coefficient, and grain size (L) for the AZO films used for optical measurements at room temperature. The seventh and eighth columns give the λ range used for the fitting and the correlation coefficients calculated by the best fit to the experimental results, respectively. L is estimated by analyzing the in-plane XRD pattern obtained by grazing XRD measurement using the Williamson-Hall plot.[37] We found the L values in the range from 35 to 41 nm of AZO films with $P_{RF}/(P_{DC}+P_{RF})$ ratio = 0 to 1.0. The oscillating motion of carrier electrons in high ($\sim 10^{14}$ Hz) frequency electric field that is represented by the optical mobility discussed in Sec. III F is confined within the grains of several tens of nanometers described above. The effect of the grain boundary on the optical mobility is thus avoided.[38]

The values of α were evaluated using the following relation:[39]

$$\alpha = \frac{1}{t}\ln\left(\frac{1-R}{T}\right), \tag{1}$$

where t is the film thickness. The exponent p for the AZO films with various power ratios was found to be from 3.09 to 3.52, as shown in Table II. This indicates that for all the AZO films in this study, the changes in the optical properties are mainly due to ionized impurity scattering.[36]

The ratio α/N for impurity scattering is theoretically given by[36]

$$\frac{\alpha}{N} = N_i\left(\frac{m}{m^*}\right)^{3/2} F(\lambda, T_{ab}), \tag{2}$$

where N_i, m, and m^* are concentration of charged centers, electron rest mass, and electron effective mass, respectively. $F(\lambda, T_{ab})$ is the function of wavelength and temperature used in the absorption measurements. We thus expected α_{1400}/N varying among the samples with various values of m^* and N_i. The experimental results obtained at room temperature indeed show such variation, as shown in Table II. With increasing power ratio, α_{1400}/N decreased from 3.59×10^{-17} to 2.01×10^{-17} cm^2. By analyzing the values of N_i

TABLE II. Process number, power ratio ($P_{RF}/(P_{DC}+P_{RF})$), carrier concentration N, absorption coefficient α_{1400}, capture cross section (α_{1400}/N), the best fitting p (details in text), fitting region, correlation coefficient, and grain size (L).

Process number	Power ratio $P_{RF}/(P_{DC}+P_{RF})$	Carrier concentration N [$\times 10^{20}$ cm^{-3}]	Absorption coefficient α_{1400} [cm^{-1}]	α_{1400}/N [$\times 10^{-17}$ cm^2]	p	Fitting region [nm]	Correlation coefficient	Grain size, L [nm]
Proc. 1	0.00	5.92	21 236	3.59	3.35	1300–1900	0.9595	35.9
Proc. 2	0.06	6.63	22 012	3.32	3.51	1300–1900	0.9547	42.8
Proc. 3	0.14	6.88	23 365	3.40	3.41	1300–1900	0.9554	39.5
Proc. 4	0.25	6.27	19 889	3.17	3.23	1350–1950	0.9557	41.7
Proc. 5	0.50	5.42	15 770	2.91	3.36	1400–2000	0.9711	38.6
Proc. 6	0.67	5.27	14 588	2.77	3.52	1400–2000	0.9753	37.6
Proc. 7	0.67	4.97	13 034	2.62	3.09	1500–2100	0.9709	35.9
Proc. 8	0.80	4.69	10 747	2.29	3.32	1500–2100	0.9825	40.6
Proc. 9	1.00	4.13	8303	2.01	3.48	1500–2100	0.9875	41.7

calculated using the theoretical expression (2) and m^* obtained by employing the expression used for linear fitting to the experimental data, $m^* = (0.280 + 0.010 \times 10^{-20} N)\, m$,[32] where m is the free-electron mass, we found that an increase in the power ratio causes N_i to decrease sharply, whereas N/N_i tends to increase as the power ratio increases. In the above calculations, we assumed that the effect of lattice scattering on α_{1400}/N is negligible compared with that of impurity scattering; this was reasonable considering the values of the exponent p for all the samples discussed above. Taking into account the fact that N_i includes the concentrations of donor-charged defects, N_D, and acceptor-charged defects, N_A, i.e., $N_i = N_D + N_A$, N/N_i can be written as

$$N/N_i = N/((1+\theta)N_D), \tag{3}$$

where θ is the compensation ratio N_A/N_D. The above finding implies that an increase in $P_{RF}/(P_{DC}+P_{RF})$ reduces not only N_D but also θ.

F. Contribution of GB scattering to carrier transport

In the following, a general discussion of the factors limiting the carrier transport of polycrystalline AZO films obtained by different deposition processes is presented. Note that AZO films are found in polycrystalline form: the films are composed of grain bulk and GBs. Carriers thus cross several grains during Hall effect measurements. The total carrier-scattering frequency (ω_{total}) is the sum of the individual frequencies due to each scattering mechanisms; ω_{total} may be expressed in terms of the two regions above by applying Matthiessen's rule[40] as

$$\omega_{total} = \tau_{ig}^{-1} + \tau_{GB}^{-1}, \tag{4}$$

where τ_{ig}^{-1} is the sum of the individual frequencies due to each scattering mechanisms in the grain bulk, including ionized impurity scattering, neutral impurity scattering, and lattice vibration scattering,[41–44] and τ_{GB}^{-1} is the scattering frequency at the GBs. In the AZO films with high N in this work, i.e., high degeneracy, only a narrow range of energy around the Fermi level is of interest. Then, on the basis of Eq. (4), μ_H ($= e/(m^*\omega_{total})$) limited by the scattering mechanisms taking place in the grain bulk and at the GBs can be expressed as[23–25]

$$\frac{1}{\mu_H} = \frac{1}{\mu_{ig}} + \frac{1}{\mu_{GB}}. \tag{5}$$

In this study, we use the μ_{opt} as μ_{ig}.[23–25] To investigate the contribution of GB scattering to carrier mobility, Eq. (5) is rewritten as follows:[24,25]

$$\frac{\mu_{opt}}{\mu_{GB}} = \frac{\mu_{opt} - \mu_H}{\mu_H}. \tag{6}$$

When $\mu_{opt}/\mu_{GB} \sim 0$, Eq. (6) shows that μ_H is practically equal to μ_{opt}. Note that to achieve AZO films with high μ_H, it is essential to enhance μ_{opt} together with little contribution of the GB scattering mechanism to carrier transport.

Using the Drude model with the Tauc-Lorentz model,[32] we estimated μ_{opt} values of the AZO films. In the following, we briefly discuss how to estimate the μ_{opt} (for details see our previous publication[33]). To describe the optical response due to free electrons, the dielectric functions for the AZO films based on the conventional Drude model (ε_D) is expressed by

$$\varepsilon_D(E) = -\frac{A_D}{E^2 - i\Gamma_D E}, \tag{7}$$

where A_D and Γ_D are the oscillator amplitude and broadening parameter, respectively, which were used as fitting parameters to reproduce the T and R spectra. A_D and Γ_D are expressed as

$$A_D = \frac{\hbar^2 e^2 N_{opt}}{m^* \varepsilon_0}, \tag{8}$$

$$\Gamma_D = \frac{\hbar e}{m^* \mu_{opt}}, \tag{9}$$

where $\hbar \equiv h/2\pi$ and h is Planck's constant. In this study, we assumed $N_{opt} = N$. Concerning m^*, we used an empirical expression.[32]

Figure 8 shows μ_{opt} and the contribution of GBs to carrier transport (μ_{opt}/μ_{GB}) as a function of $P_{RF}/(P_{DC}+P_{RF})$. μ_{opt} hardly changed regardless of the value of $P_{RF}/(P_{DC}+P_{RF})$, while μ_{opt}/μ_{GB} strongly depended on it. This clearly demonstrated that the intrinsic properties of the materials are almost constant. Also, a comparison of the behavior of μ_{opt}/μ_{GB}

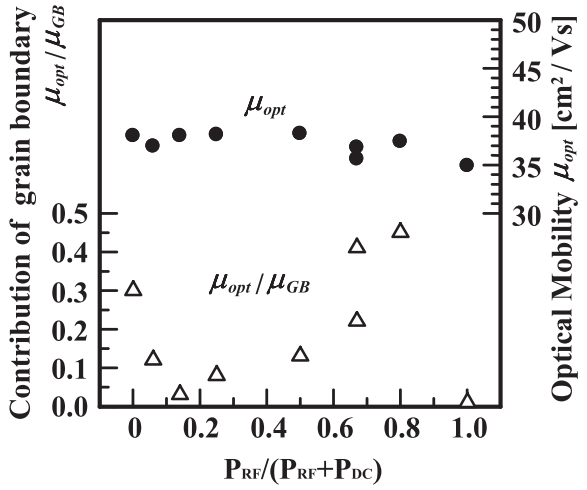

FIG. 8. Optical mobility (μ_{opt}) and contribution of grain boundaries scattering mechanism to carrier transport (μ_{opt}/μ_{GB}) of AZO films as a function of the power ratio, $P_{RF}/(P_{DC}+P_{RF})$.

against $P_{RF}/(P_{DC}+P_{RF})$ with that of μ_H (see Fig. 6(b)) proved that the dominant factor limiting the value of μ_H for the AZO films was the contribution of the scattering mechanism of GBs to carrier transport.

For the AZO films deposited with $P_{RF}/(P_{DC}+P_{RF}) = 0.14$ and 1.0, μ_{opt}/μ_{GB} had very low values of 0.03 and 0.01, respectively. These films exhibited high values of μ_H, close to their values of μ_{opt}. The AZO films deposited with $P_{RF}/(P_{DC}+P_{RF}) = 0.14$ had the highest μ_H of 36.8 cm^2/Vs together with the highest N, leading to the lowest ρ value of 2.47×10^{-4} Ωcm owing to enhanced μ_{opt} together with the very low μ_{opt}/μ_{GB}. Interestingly, the AZO films deposited with $P_{RF}/(P_{DC}+P_{RF}) = 0$ and 0.8 had large values of μ_{opt}/μ_{GB} of 0.3 and 0.45, respectively, resulting in a distinct reduction in carrier mobility (see Fig. 6(b)).

IV. SUMMARY

In this work, we investigated the structural, electrical, and optical properties of highly transparent 500-nm-thick polycrystalline AZO films on glass substrates deposited by MS with various values of $P_{RF}/(P_{DC}+P_{RF})$. The glass substrate temperature was 200 °C. We found that ρ ranged from 2.47×10^{-4} to 5.13×10^{-4} Ωcm, while the average transmittance of the glass substrates with the AZO films was more than 84% in the VIS range.

The conventional DC-MS technique, corresponding to $P_{RF}/(P_{DC}+P_{RF}) = 0$, gave rise to AZO films with a mixed grain orientation and poor c-axis alignment between the columnar grains of the polycrystalline structure, whereas the conventional RF-MS technique, corresponding to $P_{RF}/(P_{DC}+P_{RF}) = 1.0$, resulted in AZO films with a well-defined single (0001) orientation with columnar grains exhibiting a preferential c-axis orientation. The RF/DC-MS technique played an important role in enhancing the crystal quality of the polycrystalline AZO films with a preferential orientation along the c-axis perpendicular to the glass substrate. An increase in $P_{RF}/(P_{DC}+P_{RF})$ led to compressive strain along the c-axis direction but had little effect in the a-axis direction, resulting in a decrease in the V. After a careful analysis to compare the data obtained by out-of-plane and in-plane XRD measurements, we concluded that $P_{RF}/(P_{DC}+P_{RF}) = 0.14$ is a critical power ratio when describing the evolution of the structural properties of AZO films.

The electrical properties of the AZO films could be controlled by changing $P_{RF}/(P_{DC}+P_{RF})$. We found that the AZO films deposited with $P_{RF}/(P_{DC}+P_{RF}) = 0.14$ exhibited the lowest ρ value of 2.47×10^{-4} Ωcm with $N = 6.88 \times 10^{20}\,cm^{-3}$ and $\mu_H = 36.8\,cm^2/Vs$. We found that the $P_{RF}/(P_{DC}+P_{RF})$ dependence of μ_H was similar to that of N with increasing $P_{RF}/(P_{DC}+P_{RF})$ up to 0.8. Upon further increasing $P_{RF}/(P_{DC}+P_{RF})$ up to 1.0, μ_H increased abruptly, whereas N monotonically decreased.

All the AZO films in this work exhibited high transparency; an average T exceeding 84% was obtained in the VIS spectral range from 400 to 700 nm. The AZO films with $P_{RF}/(P_{DC}+P_{RF}) = 0.14$ had the highest average T of 84.7%. To investigate the dominant scattering mechanism in the grain bulk of AZO films, we analyzed the λ-dependence of α, $\alpha \propto \lambda^p$, obtained from T and R data in the NIR region, where free carrier absorption occurs. We found that the changes in the optical properties were mainly due to ionized impurity scattering as a result.

To present a more convincing argument for the factors that determine carrier transport in polycrystalline films to achieve low-ρ AZO films with high μ_H, we studied the contribution of the GBs scattering mechanism to the carrier mobility of AZO films deposited by various MS techniques. The comparison between μ_{opt} calculated by optical analysis and μ_H obtained by electrical measurements provided a comprehensive understanding of the above factors: the intrinsic electrical properties of the materials were almost constant and the dominant factor limiting the value of μ_H for the AZO films was the contribution of the scattering mechanism of the GBs to carrier transport. The AZO films with the highest N with a very low contribution of the scattering mechanism of the GBs to carrier mobility showed the lowest ρ. For the films in this work, further studies should be carried out, mainly focusing on increasing not only μ_{opt} but also the lateral grain size while maintaining low values of μ_{opt}/μ_{GB} to improve electrical conductivity.

ACKNOWLEDGMENTS

This work has been supported by Japan Society for the promotion of science JSPS (Kakenhi Grant No. 26790050), Grant-in-Aid for Young Scientists (B) under the title "The control technology and influence of the structural properties of carrier transport for impurity-doped ZnO films," and (Kakenhi Grant No. 30320120), Basic Research (A) under the title "High performance ZnO-based hydrogen gas sensor."

[1]T. Minami, MRS Bull. **25**, 38 (2000).
[2]K. Kushiya, S. Kuriyama, I. Hara, Y. Nagoya, M. Tachiyuki, and Y. Fujiwara, in *Proceedings of 29th IEEE Photovoltaic Specialists Conference* (Institute of Electrical and Electronics Engineers, New Orleans, LA, 2002), p. 579.
[3]T. Yamamoto, T. Yamada, A. Miyake, H. Makino, and N. Yamamoto, J. Soc. Inf. Display **16**(7), 713 (2008).

[4]N. Yamamoto, H. Makino, S. Osone, A. Ujihara, T. Ito, H. Hokari, T. Maruyama, and T. Yamamoto, Thin Solid Films **520**, 4131 (2012).
[5]M. J. Brett, R. W. McMahon, J. Affinito, and R. R. Parsons, J. Vac. Sci. Technol. A **1**, 352 (1983).
[6]D. J. Kang, J. S. Kim, S. W. Jeong, Y. Roh, S. H. Jeong, and J. H. Boo, Thin Solid Films **475**, 160 (2005).
[7]K. Ellmer, R. Cebulla, and R. Wendt, Thin Solid Films **317**, 413 (1998).
[8]R. Cebulla, R. Wendt, and K. Ellmer, J. Appl. Phys. **83**, 1087 (1998).
[9]M. Bender, J. Trube, and J. Stollenwerk, Thin Solid Films **354**, 100 (1999).
[10]Y.-H. Tak, K.-B Kim, H.-G. Park, K.-H. Lee, and J.-R. Lee, Thin Solid Fims **411**, 12 (2002).
[11]H.-C. Lee, Appl. Surf. Sci. **252**, 2647 (2006).
[12]M. Stowell, J. Müller, M. Ruske, M. Lutz, and T. Linz, Thin Solid Films **515**, 7654 (2007).
[13]S. I. Kim, T. D. Jung, and P. K. Song, Thin Solid Films **518**, 3085 (2010).
[14]T. Minami, T. Miyata, Y. Ohtani, and Y. Mochizuki, Jpn. J. Appl. Phys. Part 2 **45**, L409 (2006).
[15]J. Oda, J. Nomoto, T. Miyata, and T. Minami, Thin Solid Films **518**, 2984 (2010).
[16]N. Ito, N. Oka, Y. Sato, and Y. Shigesato, Jpn. J. Appl. Phys. Part 1 **49**, 071103 (2010).
[17]J. Nomoto, T. Hirano, T. Miyata, and T. Minami, Thin Solid Films **520**, 1400 (2011).
[18]N. Yamamoto, H. Makino, T. Yamada, Y. Hirashima, H. Iwaoka, T. Ito, A. Ujihara, H. Hokari, H. Morita, and T. Yamamoto, J. Electrochem. Soc. **157**, J13 (2010).
[19]A. K. Sigdel, P. F. Ndione, J. D. Perkins, T. Gennett, M. F. A. M. van Hest, S. E. Shaheen, D. S. Ginley, and J. J. Berry, J. Appl. Phys. **111**, 093718 (2012).
[20]J. B. Park, S. H. Park, and P. K. Song, J. Phys. Chem. Solids **71**, 669 (2010).
[21]V. Bhosle and J. Narayan, J. Appl. Phys. **100**, 093519 (2006).
[22]K. Ellmer and R. Mientus, Thin Solid Films **516**, 4620 (2008).
[23]I. Volintiru, M. Creatore, and M. C. M. van de Sanden, J. Appl. Phys. **103**, 033704 (2008).
[24]T. Yamada, H. Makino, N. Yamamoto, and T. Yamamoto, J. Appl. Phys. **107**, 123534 (2010).
[25]T. Yamamoto, H. Song, and H. Makino, Phys. Status Solidi C **10**, 603 (2013).
[26]G. Y. Yeom, J. A. Thornton, and M. J. Kushner, J. Appl. Phys. **65**, 3816 (1989).
[27]W. O. Hofer, Scanning Microsc. Suppl. **4**, 265 (1990).
[28]S. Ishibashi, Y. Higuchi, Y. Ota, and K. Nakamura, J. Vac. Sci. Technol. A **8**, 1403 (1990).
[29]K. S. Park and J. K. Park, Acta Mater. **47**, 2177 (1999).
[30]unpublished.
[31]A. Janotti and C. G. Van de Walle, Appl. Phys. Lett. **87**, 122102 (2005).
[32]H. Fujiwara and M. Kondo, Phys. Rev. B **71**, 075109 (2005).
[33]H. Makino, N. Yamamoto, A. Miyake, T. Yamada, Y. Hirashima, H. Iwaoka, T. Itoh, H. Hokari, H. Aoki, and T. Yamamoto, Thin Solid Films **518**, 1386 (2009).
[34]H. Y. Fan and M. Becker, in *Semiconducting Materials* (Butterworth Scientific Publications Ltd., London, 1951), p. 132.
[35]S. Visvanathan, Phys. Rev. **120**, 376 (1960).
[36]H. Y. Fan, W. Spitzer, and R. J. Collins, Phys. Rev. **101**, 566 (1956).
[37]G. K. Williamson and W. H. Hall, Acta Metall. **1**, 22 (1953).
[38]Y. Hishikawa, N. Nakamura, S. Tsuda, S. Nakano, Y. Kishi, and Y. Kuwano, Jpn. J. Appl. Phys. Part 1 **30**, 1008 (1991).
[39]I. Kim, K.-S. Lee, T. S. Lee, J.-H. Jeong, B.-K. Cheong, Y.-J. Baik, and W. M. Kim, J. Appl. Phys. **100**, 063701 (2006).
[40]C. Kittel, *Introduction to Solid State Physics* (Wiley, New York, 1996), p. 159.
[41]R. B. H. Tahar and N. B. H. Tahar, J. Appl. Phys. **92**, 4498 (2002).
[42]H. Yamada, T. Fukushima, T. Yoshimura, and N. Fujimura, J. Korean Phys. Soc. **58**, 792 (2011).
[43]J. S. Kim, J.-H. Jeong, J. K. Park, Y. J. Baik, I. H. Kim, T.-Y. Seong, and W. M. Kim, J. Appl. Phys. **111**, 123507 (2012).
[44]T. Terasako, H. Song, H. Makino, S. Shirakata, and T. Yamamoto, Thin Solid Films **528**, 19 (2013).